6th IEEE RAS/EMBS International Conference on
Biomedical Robotics and Biomechatronics (BioRob)
June 26-29, 2016. UTown, Singapore

Closed-Loop Control of a Magnetically-Actuated Catheter Using Two-Dimensional Ultrasound Images

Klaas Jelmer Boskma, Stefano Scheggi, and Sarthak Misra

***Abstract*— Robotically-actuated catheters are being employed in endovascular interventions for their improved maneuverability and steering precision over conventional catheters. Fluoroscopy is commonly used to guide such medical devices during interventions. Motivated by the limitations and hazards associated with fluoroscopy, this study investigates the use of ultrasound images as a viable alternative for the real-time visualization of a robotic catheter. In order to validate the proposed approach, an integrated system is developed which employs a two-dimensional ultrasound-based tracking algorithm to detect and track a magnetically-actuated catheter. By using Euler-Bernoulli beam theory to describe the motion of the catheter and a closed-loop control, the magnetic field steers the robotic catheter in two-dimensional space. Experiments show that the model is able to describe the catheter deflections with a fitting error of R^2 = 0.96. Closed-loop steering experiments show a maximum positioning error of 0.46 mm. Our study demonstrates the possibility to accurately steer a magnetic catheter using two-dimensional ultrasound images.**

I. Introduction

Endovascular surgery is a minimally invasive procedure in which catheters and guidewires are used to access organs and blood vessels. Catheters are steered from an insertion point to a target site, where diagnostic and therapeutic procedures are performed. Various factors determine the outcome of this procedure, such as the maneuverability of the catheter, the complexity of the vessel network and the surgeon's skill set [1]. Limited catheter maneuverability affects the procedure time and increases the risk of hematoma formation and vessel puncture [2].

Robotically-actuated catheters have been developed in order to address these drawbacks. Such medical devices can be driven by pull-wires, as demonstrated in the robotic navigation systems Sensei (Hansen Medical, Mountain View, USA) and Amigo (Catheter robotics, Mount Olive, USA). These systems allow high precision steering in the endovascular network with less X-ray exposure than conventional procedures [3], [4]. Compared to pull-wire driven actuation, magnetically-actuated catheters yield higher success rates when applied in cardiovascular interventions [5]. This form of actuation steers the catheter with high precision by interactions between permanent magnets that are embedded in the catheter and an external magnetic field. No pull-wires are required to steer the catheter, making the catheters less stiff and more maneuverable. As a result of the increased flexibility, vessel puncture and dissection are virtually impossible [6].

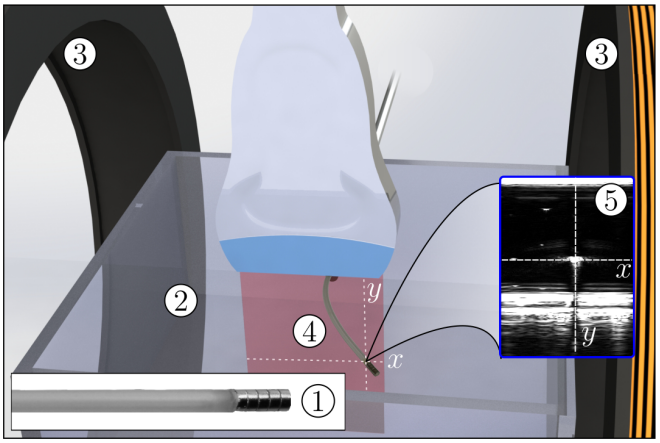

Fig. 1: A magnetic catheter (1) is inserted into an enclosed space with water (2). A magnetic field generated by Helmholtz coils (3) induces a torque on the catheter tip. The catheter displacement (4) is detected and tracked using two-dimensional ultrasound images (5).

Apart from the actuator mechanism, another key aspect of a robotic navigation system is the imaging modality which visualizes the catheter so it is distinguishable from its surrounding anatomy. Moreover, the imaging modality must be able to visualize the vascular anatomy [7]. In many clinically-available robotic navigation systems, fluoroscopy is used as the main imaging modality [8]. It has the advantage of having a high image acquisition rate. However, it provides two-dimensional (2D) projection images with low tissue contrast and the prolonged X-ray exposure poses a health risk. In order to reduce X-ray exposure, electromagnetic positioning has been used to detect the catheter position [9], [10]. However, clinically-available robotic navigation systems still rely on fluoroscopy to visualize tissue and detect the position of the catheter with respect to the surrounding environment.

Magnetic resonance (MR) has been investigated as an alternative imaging modality for visualizing robotic catheters [11]. It offers several advantages over fluoroscopy, such as high contrast for soft tissue, three-dimensional (3D) volumetric image reconstruction and the lack of ionizing radiation. However, MR has a low image acquisition rate and it is not compatible

K.J. Boskma and S. Misra are affiliated with the Surgical Robotics Laboratory, Department of Biomedical Engineering, University of Groningen and University Medical Centre Groningen, 9713 GZ, The Netherlands. S. Scheggi and S. Misra are affiliated with the Surgical Robotics Laboratory, Department of Biomechanical Engineering, MIRA - Institute for Biomedical Technology and Technical Medicine, University of Twente, 7522 NB, The Netherlands. This project (ROBOTAR) has received funding from the European Research Council (ERC) under the European Union's Horizon 2020 Research and Innovation programme (Grant Agreement #638428). This work was also supported by funds from the Netherlands Organization for Scientific Research (NWO) Innovative Medical Devices Initiative (IMDI) - Project: USE (Ultrasound Enhancement).

with many conventional catheters, ferromagnetic materials and electrical components, and thereby imposes additional challenges for the design of MR-guided robots [12], [13].

The use of ultrasound (US) as an imaging modality for robotic catheters seems unexplored [8]. US transducers are able to provide 2D and 3D images with a high frame acquisition rate, which can be beneficial to interventions in dynamic environments. In this paper, US is investigated as a viable imaging modality for real-time visualization of a magnetically-actuated catheter. In order to validate the proposed approach, an experimental setup (Fig. 1) is developed in which a magnetic catheter can be steered under real-time US guidance. To the best of our knowledge, this is the first example of closed-loop control of a magnetically-actuated catheter using 2D US images.

A. Related work

Robotic catheters with embedded electromagnets and permanent magnets have previously been described in several studies. Although kinematic models have shown to accurately describe catheter deflections, none of these studies steered the catheter under US guidance.

Catheters with embedded current-carrying micro-coils were manufactured by winding thin copper wire around the distal end of the shaft [14]. When excited, the micro-coils exhibited a magnetic moment which was used to steer the catheter in the magnetic field of an MR-bore. A 3D kinematic model of such catheter is described by Liu *et al* [15]. The shaft displacement and torsions induced by the micro-coils were computed with a finite difference approach. Another approach to model a magnetic catheter is described by Lillaney *et al.*, who used Euler-Bernoulli beam theory to model the catheter as a cantilever beam [16]. The mechanical moment induced by the micro-coils was assumed to be in equilibrium with the internal bending moment. Catheters with embedded permanent magnets can be actuated by controlling the direction and strength of an external magnetic field [17]. Permanent magnets exhibit a non-decaying magnetization and do not require currents to generate a magnetic moment [18]. Therefore, permanent magnets allow for a less complex design compared to catheters with embedded micro-coils.

Gang *et al.* described a system that consisted of eight electromagnets which controlled the magnetic field strength and orientation in 3D-space [19]. Clinically relevant steering tasks were performed using a catheter with embedded permanent magnets. Similar systems were described by Le *et al.* and Ullrich *et al.*, who steered a catheter and a probe for capsulorhexis using magnetic fields respectively [20], [21]. In these studies, a kinematic model of the devices was derived and validated using optical camera images. Furthermore, in the study of Ullrich *et al.*, the tracked position of the device was used for closed-loop control. Unlike the homogeneous field present in MR systems, the high gradients generated by such coil systems are complex to model.

Regarding the US imaging modality, the majority of the literature discusses the visualization of conventional catheters that are manually steered using pull-wires. In cardiac interventions the use of 2D intracardiac echocardiography and 3D transesophageal echocardiography for catheter and tissue visualization are well established [22], [23]. A robotic catheter, capable of exerting a constant pressure on a moving heart wall under 3D US has been demonstrated [24]. Although the catheter was actuated in only one degree of freedom, both the heart wall and the robotic catheter were tracked with a frequency of 28 Hz. Both device and tissue tracking with 3D US has been demonstrated [25]. The position and orientation of a cylindrical surgical instrument was estimated by detecting and tracking passive markers on the surface of the instrument.

B. Contributions

Different from the aforementioned studies, this work demonstrates the use of 2D US to control a magnetically-actuated catheter in a stationary environment. A magnetic catheter prototype is developed with a permanent magnet attached to the distal end of the shaft. A model characterizes the deflections of the catheter using Euler-Bernoulli beam theory. Along with this model, we integrate a real-time, 2D US tracking algorithm with a system that is able to generate homogeneous magnetic fields on two axes. A feed forward controller estimates the actuation parameters while a PI (Proportional-Integral) controller compensates for the inaccuracies of the model and for external disturbances. The steering precision of the catheter is evaluated by actuating the tip along a reference trajectory.

The rest of the paper is organized as follows: Section II presents the model of the catheter used in this study. Section III describes the control system which detects the radial cross-section of the catheter in US images and actuates the catheter in a closed-loop manner. Section IV reports the results of the experimental validations while in Section V the conclusions and subjects for future work are outlined.

II. Catheter model

The catheter prototype (Fig. 2) consists of a 55 mm long flexible hollow PVC tube with an outer diameter of 2 mm and an inner diameter of 1.2 mm. A stack of 5 cylindrical Neodymium N48 (Supermagnete, Gottmadingen, Germany) magnets (2 mm diameter, 1 mm height) is attached to the distal end of the shaft. The magnets are modeled as a single dipole magnet with a remanent magnetization $B_{res} = 1.4$ T that is in-line with the longitudinal axis of the shaft [26]. In order to control the catheter in an accurate and predictable way, it is important to model its deflection in the presence of a magnetic field. A wrench ($\mathbf{W}^m \in \mathbb{R}^6$) is induced on the tip of the catheter when the magnet is in the presence of a magnetic field:

$$\mathbf{W}^m = \begin{bmatrix} \mathbf{F}^m \\ \mathbf{T}^m \end{bmatrix} = \begin{bmatrix} \nabla(\mathbf{m} \cdot \mathbf{B}) \\ \mathbf{m} \times \mathbf{B} \end{bmatrix}, \tag{1}$$

where $\mathbf{F}^m \in \mathbb{R}^3$ is the force acting on the tip, $\mathbf{T}^m \in \mathbb{R}^3$ is the torque acting on the tip, $\mathbf{m} \in \mathbb{R}^3$ is the magnetic moment vector of the magnet and ∇ is the gradient of the field. Since

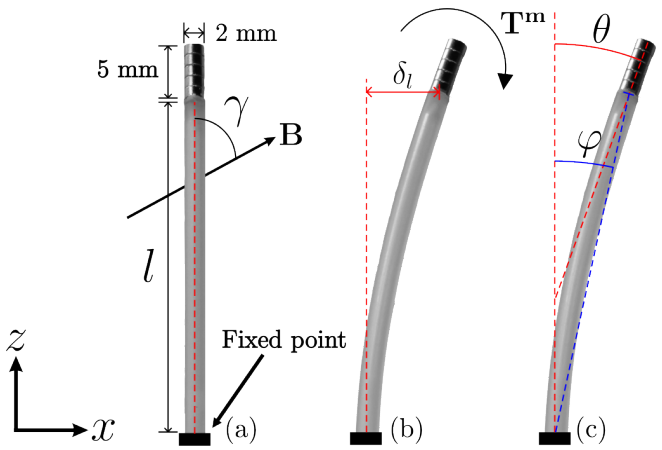

Fig. 2: Interactions of the catheter with a magnetic field ($\mathbf{B} \in \mathbb{R}^3$). (a) The catheter consists of a flexible shaft with length l = 55 mm and a permanent magnet that is attached to the distal end of the shaft. The angle γ is defined as the angle between the resting position of the catheter and the direction of the magnetic field. (b) When exposed to a magnetic field, the magnet will induce a torque ($\mathbf{T}^m$) on the tip and a displacement (δ_l) is observed at the distal end of the flexible shaft. (c) The tip deflection angle (θ) and catheter deflection angle (φ) are observed.

the generated fields in this setup are homogeneous, $\mathbf{F}^m$ is assumed to be zero. The torque tends to align the tip of the catheter with the magnetic field and it is balanced against the internal bending moment of the flexible shaft attempting to return to its resting position. An equilibrium is established when the magnitude of the torque induced by the magnet $\mathbf{T}^m$ is equal to the counteracting magnitude of the internal bending moment $\mathbf{T}^{mech}$:

$$\|\mathbf{T}^m\| = \|\mathbf{T}^{mech}\|. \tag{2}$$

The torque magnitude $\|\mathbf{T}^m\|$ can be written as the torque exerted on a permanent magnet in a magnetic field:

$$\|\mathbf{T}^m\| = \|\mathbf{m}\| \ \|\mathbf{B}\| \ \sin(\gamma - \theta), \tag{3}$$

where γ is the initial angle of the catheter with respect to $\mathbf{B}$ and θ is the tip deflection angle. The magnetic moment is computed as $\|\mathbf{m}\| = MV$, where $M = B_{res}/\mu_0$ denotes the magnetization, $\mu_0 = 4\pi \cdot 10^{-7}$ is the permeability of free space, and V is the volume of the magnet. The catheter is modeled as a cantilever beam with small deflections [27]. An analytical solution is derived from the Euler-Bernoulli bending moment-curvature relationship which is valid for deflections where $\cos(\theta) \simeq 1$. A relationship is obtained between θ and the magnitude of $\mathbf{T}^m$ acting on the free end of a cantilever with length l [16]:

$$\theta = \frac{\|\mathbf{T}^m\| l}{EI}, \tag{4}$$

where E denotes the elasticity modulus and I denotes the area moment of inertia of the cross-section of the catheter shaft. The displacement δ (Fig. 2) can be found by integrating Eq. (4) over the length of the beam so that:

$$\delta(k) = \frac{\|\mathbf{T}^m\| k^2}{2EI}, \tag{5}$$

where $0 \leq k \leq l$. This establishes a relation between the moment acting on the tip and the displacement observed at a length k. The catheter deflection φ can be computed:

$$\varphi = \tan^{-1}\left(\frac{\delta(l)}{l}\right). \tag{6}$$

By substituting Eq. (3) and Eq. (4) into Eq. (2), an equation can be obtained which is linear with respect to the field strength:

$$\frac{\theta}{\sin(\gamma - \theta)} = \frac{\|\mathbf{m}\| \ \|\mathbf{B}\| \ l}{EI}. \tag{7}$$

This relationship can be used to validate the model against experimentally obtained deflections. For a measured catheter deflection, $\theta / \sin(\gamma - \theta)$ can be computed and subsequently be compared to the model quantity $(\|\mathbf{m}\| \ \|\mathbf{B}\| \ l)/(EI)$. Using Eq. (5) we can describe the displacement of the catheter as a function of the magnetic field strength in the workspace.

III. Experimental Setup

In this section, the experimental setup used to validate the model of the catheter is introduced. Furthermore, the algorithm to detect the cross-section of the catheter and the closed-loop control policy are described.

A. Magnetic field equations

The experimental setup is reported in Fig. 3. Two pairs of Helmholtz coils generate a homogeneous magnetic field along the x- and y-axis of the system. The physical properties of the coils along the y-axis (Teltron Helmholtz Coils S, 3B scientific, Hamburg, Germany) and x-axis are listed in Table I. The field strength ($\mathbf{B} \in \mathbb{R}^2$, where $\mathbf{B} = [B_x \ B_y]^T$) in the workspace can be modeled for each coil:

$$\mathbf{B} = \left(\frac{4}{5}\right)^{\frac{3}{2}} \frac{\mu_0 n I}{R} \hat{\mathbf{v}}, \tag{8}$$

where n is the number of windings on each coil, I is the current, R is the coil radius and $\hat{\mathbf{v}} \in \mathbb{R}^2$ is an unit vector denoting the orientation of the coil pair. Each coil pair generates a field strength between -6 mT and 6 mT. The accuracy of the model described in Eq. (8) is determined by exposing a teslameter (3MH3A, Senis AG, Baar, Switzerland) to 20 field strengths within the operating range for each coil pair. An average deviation of 0.14 mT $\pm$ 0.13 mT between the modeled and measured field strength is found.

B. Catheter cross-section detection

A 14 MHz US transducer (L14-5/38, Ultrasonix, Richmond, Canada) is oriented perpendicular to the longitudinal axis of the shaft. The radial cross-section of the distal end of the shaft is visualized as a circular or oval shape (Fig. 3). 2D digital Radio Frequency (RF) frames are transmitted

TABLE I: Properties of the Helmholtz coils. The field strength is calculated using Eq. (8).

Coil	Effective radius	Coil windings	Field strength
x-axis	92.5 mm	420 turns	4.10 mT/A
y-axis	68.5 mm	320 turns	4.23 mT/A

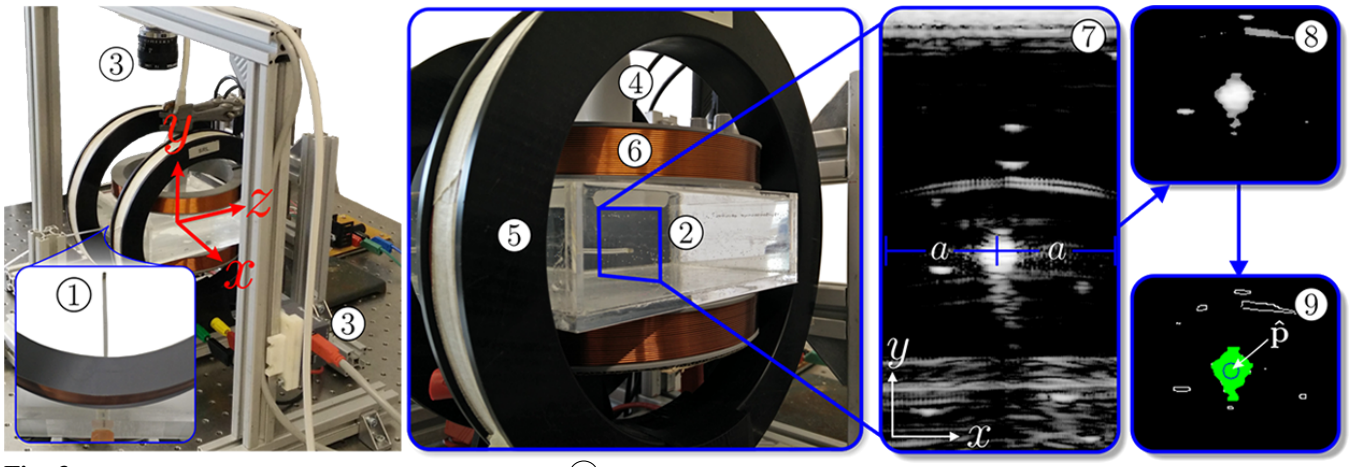

Fig. 3: Overview of the experimental setup. A catheter (1) is inserted in a water tank so that the tip of catheter is at the center of the workspace (2). The catheter is observed by two optical cameras (3) and a US transducer (4). An homogeneous magnetic fields is generated by coils on the x-axis (5) and y-axis (6). The tracking method, which is described in Section III-B, exploits temporal continuity to speed up the detection procedure. Given the estimation of the position of the catheter tip for the previous frame, the RF-lines that are within preset range (a) from that estimation are kept (7), whereas the remaining pixels are set to zero. Speckle noise and reflection artifacts are removed (8) and a contour-finding technique estimates the position ($\hat{\mathbf{p}} = [\hat{p}_x, \hat{p}_y,]^T$) of the cross-section of the catheter (9).

from the Ultrasound Research Interface present on the SonixTouchQ+ (Ultrasonix) to a workstation (3.2 GHz Intel I5, 8 GB RAM, 64 bit Windows 7). The retrieved data contains 256 beam-formed RF-lines. Each line corresponds to the signal received from an element of the US transducer. Before the catheter cross-section can be detected, a B-mode image has to be constructed from the RF-data. The delay that is caused by this computationally intensive process has a negative impact on the performance of the control system. An algorithm (Fig. 3 (7) - (9)) is implemented to reduce the image construction latency by selecting a subset of RF-lines which is then converted to an 8-bit B-mode image using the Amplio library provided by Ultrasonix. In order to obtain a distinct contour of the cross-section of the catheter, the B-mode image is pre-processed in two steps using the OpenCV computer vision library [28]. At first, speckle noise is removed using blur, dilation and erosion filters. Then, reflection artifacts are removed using a threshold filter that discards all the pixels whose values are below 200. In order to find the contours of the cross-section, a Canny edge detection operator is applied to the image, and a series of contours is obtained using a contour finding algorithm. For each contour its center-of-mass is calculated, and the estimated position of the cross-section of the catheter ($\hat{\mathbf{p}}$) is defined as the center-of-mass point with the lowest distance to the previous estimated position.

C. Ultrasound-guided actuation

The closed-loop controller (Fig. 4) is used to steer the catheter along a pre-defined reference trajectory. The model as described in Section II, estimates the field strength ($\mathbf{B}$) for a given target position ($\mathbf{p}$). The model may be inaccurate or external disturbances may be present which will result in an error ($\mathbf{e}$) between the tracked and target position. A PI controller minimizes the error by providing closed-loop control. Due to the bending stiffness of the catheter shaft, the catheter responds slowly to a change in the magnetic field strength. Therefore, no derivative term is set in the feedback loop.

IV. Experimental validation

This section presents the validation of the model derived in Section II. Furthermore, experimental results of the control policy used to steer the catheter along a path are presented.

A. Model validation

The coil pairs have different dimensions and number of windings, therefore the model is validated separately for deflections induced on the x- and y-axis. The catheter is exposed to eight field strengths within the operating range. The tip deflection angle (θ) and catheter deflection angle (φ) are observed in the xz-plane when the x-coil pair is actuated, and in the yz-plane when the y-coil pair is actuated. All deflections are measured five times with optical cameras. The deflection value $\theta / \sin(\gamma - \theta)$ is calculated

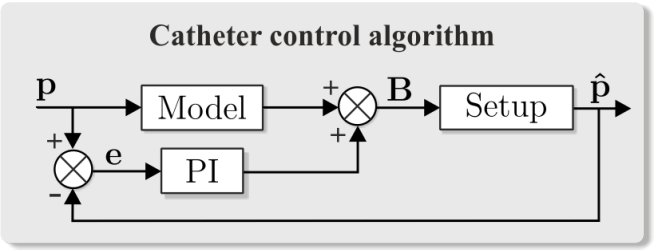

Fig. 4: The control system uses the model of the catheter in a feed forward configuration. A PI controller ($P = 1$, $I = 0.5$) is used to perform closed-loop control. Using the target position ($\mathbf{p} \in \mathbb{R}^2$, where $\mathbf{p} = [p_x, p_y]^T$), the magnetic field strength ($\mathbf{B}$) is computed as the sum of the outputs of the PI- and feed forward controller. The tracked radial cross-section of the catheter shaft is denoted by $\hat{\mathbf{p}}$. The resulting positioning error ($\mathbf{e} \in \mathbb{R}^2$, where $\mathbf{e} = \mathbf{p} - \hat{\mathbf{p}}$) is used in a PI system to perform closed-loop control.

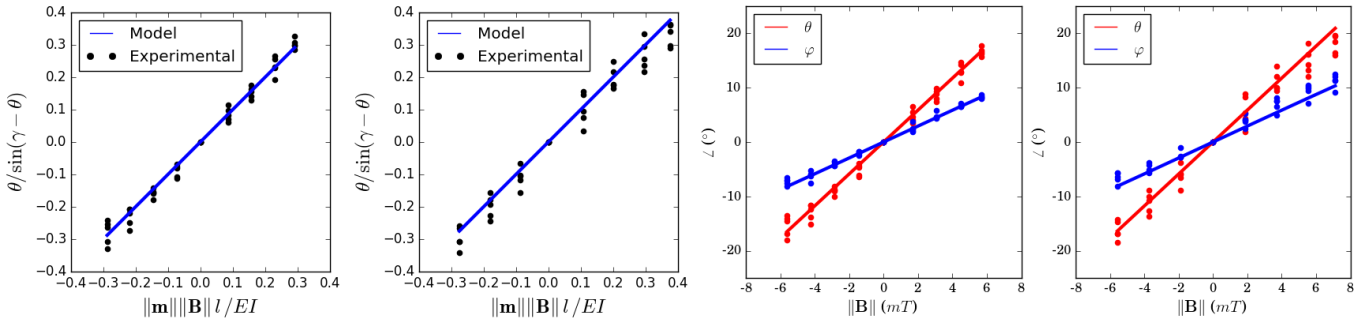

(a) R^2 = 0.99 **(b)** R^2 = 0.96 **(c)** θ R^2=0.99, φ R^2 = 0.99. **(d)** θ R^2 = 0.97, φ R^2 = 0.95

Fig. 5: The model is validated for the (a) x-axis and (b) y-axis. Deflection value $\theta/\sin(\gamma-\theta)$ is calculated for each measurement and plotted against the expected value $(\|\mathbf{m}\|\ \|\mathbf{B}\|\ l)/(EI)$. The measurements (dots) and model prediction (line) are shown. Deflection angles θ and φ are plotted for measurements on the (c) x-axis and (d) y-axis. Measured angles (dots) and the model predictions (lines) are shown.

for each measurements and plotted against the expected values provided by the model $(\|\mathbf{m}\|\ \|\mathbf{B}\|\ l)/(EI)$. The accuracy of the model is determined by how well the model explains the variability in the experimental data. Prior to the experiments, the catheter is oriented so that γ is equal to 90° (Fig. 2) Since the bending stiffness (EI) is unknown for the shaft material, 10 different deflections are measured using optical cameras in both the xz and yz planes so that Eq. (7) can be solved for EI. An average bending stiffness of $17.85 \cdot 10^{-6} \pm 2.45 \cdot 10^{-6}$ Nm^2 is obtained.

The results of the model validation experiments are shown in Figs. 5(a) and 5(b). A model fit of R^2=0.99 and R^2=0.96 is found for deflections using the x- and y-coil pairs respectively. Due to the limited size of the workspace, the catheter comes in contact with the water tank if the coil pair on the y-axis generates a field strength lower than -6 mT. These measurements are not used in the evaluation of the model. The comparison between the tip angle (θ) and catheter angle (φ) is shown in Figs. 5(c) and 5(d). Both the experimental data and the model show that the tip angle is consistently larger than the catheter angle. Tip deflections from -18° to 18° and catheter deflections from -6° to 6° are observed in the xz-plane, and fit the model with R^2=0.99 for both θ and φ. A similar relation between the tip angle and catheter angle is found for measurements in the yz-plane, but the model has a worse fit of R^2=0.97 and R^2=0.95 for θ and φ respectively. This could be a result of the gravity acting on the tip, resulting in different bending characteristics between positive and negative deflections on the y-axis.

B. Closed-loop control using ultrasound images

The closed-loop performance of the system is evaluated by steering the catheter tip along reference trajectories in the shape of a square, rhombus, circle and figure-eight. The reference square path has edges of 14 mm, the rhombus has edges of 10 mm, the circle has a radius of 7 mm and the figure-eight has sides of 14 mm. All trajectories are evaluated with an actuating tip velocity of 1 mm/s. A preset range a = 20 is selected for the cross-section detection algorithm so that a total of 40 RF-lines are used for each B-mode image. US images are acquired with a frame rate of 43Hz. The results of the trajectory steering experiments are presented in Fig. 6. In all of the figures a shape slightly larger than the reference trajectory is observed. The tracked position of the tip shows spikes, which are caused by inaccuracies in the US tracking algorithm. Since the acquired US images are two dimensional, only the xy-plane is observed, and the out-of-plane motion of the tip cannot be detected. Hence, when the catheter is deflected, the cross-section of a segment different from the distal end of the shaft is detected. The estimated out-of-plane movement is 0.5 mm. As a consequence, the tracked tip position may deviate from the actual tip position. The steering experiments in this study took place in a stationary environment, which is a simplification of complex scenarios such as a beating heart. When tracking a catheter under US guidance in such an environment, additional tracking uncertainties may arise due to the reduced visibility of the catheter [25].

V. Conclusions and Future Work

This study presents a novel approach to steer a magnetically-actuated catheter by using a closed-loop control and US images. A model of the catheter is derived that computes the field strength necessary to bend the catheter. The integrated system is able to autonomously detect and track the cross-section of the catheter and uses this information to robustly control the tip of the catheter in a closed-loop manner.

In future studies we plan to extend the proposed tracking and control system with a 3D US imaging system [29]. The position of the catheter can then be detected in three dimensions with sub-millimeter precision. Moreover, we will address the limited applicability of Euler-Bernoulli beam theory to describe catheter deflections by extending it with a finite element approach. By performing steering experiments in US-compatible vascular and cardiac phantoms, we plan to evaluate the performance of the integrated system in clinically-relevant scenarios.

References

[1] Y. Fu, H. Liu, W. Huang, S. Wang, and Z. Liang, "Steerable catheters in minimally invasive vascular surgery," *International Journal of Medical Robotics and Computer Assisted Surgery*, vol. 5, no. 4, pp. 381–391, 2009.

[2] F. P. Gosselin, V. Lalande, and S. Martel, "Characterization of the deflections of a catheter steered using a magnetic resonance imaging system," *Medical Physics*, vol. 38, no. 9, pp. 4994–5002, 2011.

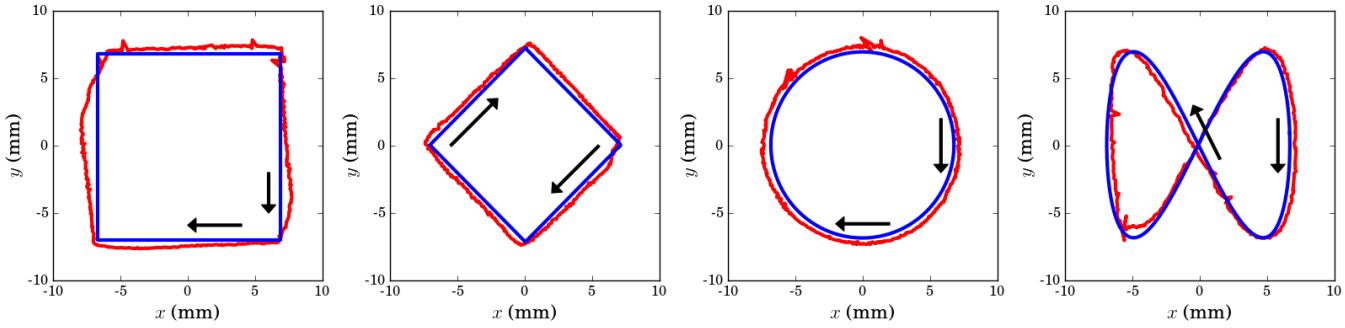

(a) Square path. $\epsilon_x = 0.39 \pm 0.003$, $\epsilon_y = 0.33 \pm 0.003$

(b) Rhombus path. $\epsilon_x = 0.42 \pm 0.006$, $\epsilon_y = 0.40 \pm 0.001$

(c) Circular path. $\epsilon_x = 0.30 \pm 0.010$, $\epsilon_y = 0.30 \pm 0.002$

(d) Figure-eight path. $\epsilon_x = 0.53 \pm 0.006$, $\epsilon_y = 0.79 \pm 0.008$

Fig. 6: Closed-loop control results for the magnetic catheter tip following a (a) square, (b) rhombus, (c) circular and (d) figure-eight path. The reference trajectory (blue) and detected position using US images (red) are shown. The average position errors ϵ_x [mm] and ϵ_y [mm] and their standard deviation over three experiments are reported. Refer to the accompanying video that demonstrates the real-time catheter control using US images.

[3] E. M. Khan, W. Frumkin, G. A. Ng, S. Neelagaru, F. M. Abi-Samra, J. Lee, M. Giudici, D. Gohn, R. A. Winkle, J. Sussman, B. P. Knight, A. Berman, and H. Calkins, "First experience with a novel robotic remote catheter system: Amigo mapping trial," *Journal of Interventional Cardiac Electrophysiology*, vol. 37, no. 2, pp. 121–129, 2013.

[4] G. A. Antoniou, C. V. Riga, E. K. Mayer, N. J. W. Cheshire, and C. D. Bicknell, "Clinical applications of robotic technology in vascular and endovascular surgery," *Journal of Vascular Surgery*, vol. 53, no. 2, pp. 493–499, 2011.

[5] S. H. Kim, Y. S. Oh, D. H. Kim, I. J. Choi, T. S. Kim, W. S. Shin, J. H. Kim, S. W. Jang, M. Y. Lee, and T. H. Rho, "Long-term outcomes of remote magnetic navigation for ablation of supraventricular tachycardias," *Journal of Interventional Cardiac Electrophysiology*, vol. 43, no. 2, pp. 187–192, 2015.

[6] S. Ernst, "Magnetic and robotic navigation for catheter ablation: "Joystick ablation"," *Journal of Interventional Cardiac Electrophysiology*, vol. 23, no. 1, pp. 41–44, 2008.

[7] Y. Ganji, F. Janabi-Sharifi, and A. N. Cheema, "Robot-assisted catheter manipulation for intracardiac navigation," *International Journal of Computer Assisted Radiology and Surgery*, vol. 4, no. 4, pp. 307–315, 2009.

[8] H. Rafii-Tari, C. J. Payne, and G. Z. Yang, "Current and emerging robot-assisted endovascular catheterization technologies: A review," *Annals of Biomedical Engineering*, vol. 42, no. 4, pp. 697–715, 2014.

[9] A. Al-Ahmad, J. D. Grossman, and P. J. Wang, "Early experience with a computerized robotically controlled catheter system," *Journal of Interventional Cardiac Electrophysiology*, vol. 12, no. 3, pp. 199–202, 2005.

[10] T. Krings, J. Finney, P. Niggemann, P. Reinacher, N. Lück, A. Drexler, J. Lovell, A. Meyer, R. Sehra, P. Schauerte, M. Reinges, F. J. Hans, and A. Thron, "Magnetic versus manual guidewire manipulation in neuroradiology: In vitro results," *Neuroradiology*, vol. 48, no. 6, pp. 394–401, 2006.

[11] P. Moftakhar, P. Lillaney, A. D. Losey, D. L. Cooke, A. J. Martin, B. R. H. Thorne, R. L. Arenson, M. Saeed, M. W. Wilson, and S. W. Hetts, "New-Generation Laser-lithographed Dual-Axis Magnetically Assisted Remote-controlled Endovascular Catheter for Interventional MR Imaging: In Vitro Multiplanar Navigation at 1.5 T and 3 T versus X-ray Fluoroscopy," *Radiology*, vol. 277, no. 3, pp. 842–52, 2015.

[12] M. Bock and F. K. Wacker, "MR-guided intravascular interventions: Techniques and applications," *Journal of Magnetic Resonance Imaging*, vol. 27, no. 2, pp. 326–338, 2008.

[13] L. Muller, M. Saeed, M. W. Wilson, and S. W. Hetts, "Remote control catheter navigation: options for guidance under MRI," *Journal of Cardiovascular Magnetic Resonance*, vol. 14, no. 1, p. 33, 2012.

[14] N. Gudino, J. A. Heilman, J. J. Derakhshan, J. L. Sunshine, J. L. Duerk, and M. A. Griswold, "Control of intravascular catheters using an array of active steering coils," *Medical Physics*, vol. 38, no. 7, pp. 4215–4224, 2011.

[15] T. Liu and M. C. Cavusoglu, "Three dimensional modeling of an MRI actuated steerable catheter system," in *Proceedings of IEEE International Conference on Robotics and Automation (ICRA)*, 2014, pp. 4393–4398.

[16] P. Lillaney, C. Caton, A. J. Martin, A. D. Losey, L. Evans, M. Saeed, D. L. Cooke, M. W. Wilson, and S. W. Hetts, "Comparing deflection measurements of a magnetically steerable catheter using optical imaging and MRI," *Medical Physics*, vol. 41, no. 2, p. 22305, 2014.

[17] A. Ali, D. H. Plettenburg, and P. Breedveld, "Steerable Catheters in Cardiology : Classifying Steerability and Assessing Future Challenges," *IEEE Transactions on Biomedical Engineering*, vol. 63, no. 4, pp. 679–693, 2016.

[18] J. C. H. Chu, W. C. Hsi, L. Hubbard, Y. Zhang, D. Bernard, P. Reeder, and D. Lopes, "Performance of magnetic field-guided navigation system for interventional neurosurgical and cardiac procedures," *Journal of Applied Clinical Medical Physics*, vol. 6, no. 3, pp. 143–149, 2005.

[19] E. S. Gang, B. L. Nguyen, Y. Shachar, L. Farkas, L. Farkas, B. Marx, D. Johnson, M. C. Fishbein, C. Gaudio, and S. J. Kim, "Dynamically shaped magnetic fields: Initial animal validation of a new remote electrophysiology catheter guidance and control system," *Circulation: Arrhythmia and Electrophysiology*, vol. 4, no. 5, pp. 770–777, 2011.

[20] V. N. T. Le, N. H. Nguyen, K. Alameh, R. Weerasooriya, and P. Pratten, "Accurate modeling and positioning of a magnetically controlled catheter tip," *Medical Physics*, vol. 43, no. 2, pp. 650–663, 2016.

[21] F. Ullrich, S. Schuerle, R. Pieters, and A. Dishy, "Automated Capsulorhexis Based on a Hybrid Magnetic-Mechanical Actuation System," in *Proceedings of IEEE International Conference on Robotics and Automation (ICRA)*, 2014, pp. 4387–4392.

[22] E. Altiok, M. Becker, S. Hamada, E. Grabskaya, S. Reith, N. Marx, and R. Hoffmann, "Real-time 3D TEE allows optimized guidance of percutaneous edge-to-edge repair of the mitral valve," *JACC. Cardiovascular imaging*, vol. 3, no. 11, pp. 1196–1198, 2010.

[23] T. Bartel, S. Müller, A. Biviano, and R. T. Hahn, "Why is intracardiac echocardiography helpful? Benefits, costs, and how to learn," *European Heart Journal*, vol. 35, no. 2, pp. 69–76, 2014.

[24] S. B. Kesner and R. D. Howe, "Robotic catheter cardiac ablation combining ultrasound guidance and force control," *The International Journal of Robotics Research*, vol. 33, no. 4, pp. 631–644, 2014.

[25] J. Stoll, H. Ren, and P. E. Dupont, "Passive markers for tracking surgical instruments in real-time 3-D ultrasound imaging," *IEEE Transactions on Medical Imaging*, vol. 31, no. 3, pp. 563–575, 2012.

[26] Supermagnete, *Technical data and application safety, S-02-01-N datasheet*, 2011.

[27] T. Beléndez, C. Neipp, and A. Beléndez, "Large and small deflections of a cantilever beam," *European Journal of Physics*, vol. 23, no. 3, pp. 371–379, 2002.

[28] G. Bradski, "Open source computer vision," *Dr. Dobb's Journal of Software Tools*, 2000.

[29] M. Abayazid, G. J. Vrooijink, S. Patil, R. Alterovitz, and S. Misra, "Experimental evaluation of ultrasound-guided 3D needle steering in biological tissue," *International Journal of Computer Assisted Radiology and Surgery*, vol. 9, no. 6, pp. 931–939, 2014.